An adaptive, fully implicit multigrid phase-field model for the quantitative simulation of non-isothermal binary alloy solidification

J. Rosam[a,b], *P.K. Jimack*[b] *& A.M. Mullis*[a*]

[a]Institute for Materials Research, University of Leeds, Leeds LS2 9JT, UK

[b]School of Computing, University of Leeds, Leeds LS2 9JT, UK

Abstract

Using state-of-the-art numerical techniques, such as mesh adaptivity, implicit time-stepping and a non-linear multi-grid solver, the phase-field equations for the non-isothermal solidification of a dilute binary alloy have been solved. Using the quantitative, thin-interface formulation of the problem we have found that at high Lewis number a minimum in the dendrite tip radius is predicted with increasing undercooling, as predicted by marginal stability theory. Over the dimensionless undercooling range 0.2-0.8 the radius selection parameter, σ^*, was observed to vary by over a factor of 2 and in a non-monotonic fashion, despite the anisotropy strength being constant.

1. Introduction

One of the most fundamental and all-pervasive microstructures produced during the solidification of metals is the dendrite. Remnants of these dendritic microstructures often survive subsequent processing operations, such as rolling and forging, and the length scales established by the dendrite can influence not only the final grain size but also micro- and hence macro-segregation patterns. This can have a wide-ranging influence on both the properties of finished metallic products, affecting for instance mechanical properties,

* Corresponding author. E-mail: A.M.Mullis@leeds.ac.uk

corrosion resistance and surface finish, and on the formability of metallic feedstock, such as the ability to resist hot tearing during rolling.

Where dendritic growth has been observed directly, in transparent analogue casting systems such as succinonitrile [1] and xenon [2], the evidence is that the morphology of dendrites grown at different undercoolings is probably self-similar when scaled against the tip radius, ρ. Consequently all the more obvious length scales of the dendrite are simple multiples of ρ, thus making the ability to predict ρ accurately a problem of central importance to the theory of dendritic growth.

The problem of predicting ρ first became apparent in 1947 when Ivantsov [3] showed that an isothermal paraboloid of revolution, growing at velocity V into an undercooled melt, was a shape-preserving solution to the diffusion equation, thus giving rise to the idea of the parabolic needle dendrite. The analytical solution for such a crystal growing into its undercooled melt is degenerate in that it relates the Peclet number, and not the growth velocity, to undercooling, where the Peclet number is defined as

$$Pt = \frac{V\rho}{2\alpha}, \tag{1}$$

with α the thermal diffusivity in the melt. Consequently, at a given undercooling an infinite set of solutions is admissable, subject to the condition $V\rho$ = constant. Such degeneracy is not observed in nature, where a well-defined growth velocity can always be associated with a given undercooling, thus sparking the search for an additional mechanism to set the length scale, ρ, for the dendrite.

One of the most enduring solutions to this problem is based on a linear stability analysis of a plane solidification front against the growth of small perturbations [4]. This theory postulates that the dendrite grows at the largest value of ρ which is stable against small perturbations in the growth (as such perturbations would cause tip splitting and hence reduce

ρ), i.e. at the limit of marginal stability. The principal prediction of this theory is that capillary forces break the Ivantsov degeneracy via the relationship:

$$\rho^2 V = \frac{2\alpha d_o}{\sigma^*}, \tag{2}$$

where d_o is a capillary length. σ^* is the so-called stability constant, which for a plane interface is given by Mullins and Sekerka [4] as $\sigma^* = 1/(4\pi^2) \approx 0.0253$.

This theory, particularly in its more sophisticated forms due to Lipton, Glicksman and Kurz (LGK) [5, 6] and Lipton, Kurz and Trivedi (LKT) [7], was reasonably successful in fitting experimentally determined velocity–undercooling data [8]. Moreover, direct simultaneous measurement of V and ρ for succinonitrile [9] yields an experimental value for σ^* in this system of 0.0195, in close agreement with theory. However, despite this the theoretical basis of the marginal stability hypothesis must be considered somewhat ad hoc. In particular, boundary integral methods [10, 11] (microscopic solvability theory) have shown that the Ivantsov equations have no solution in the absence of crystalline anisotropy, and therefore the apparent agreement between marginal stability theory and experiment is fortuitous. The full analysis reveals that in the limit of low Peclet numbers an equation similar to the one arising from marginal stability is encountered but that σ^* is the anisotropy-dependant eigenvalue for the problem, which for small Peclet numbers is found to vary as $\sigma^*(\varepsilon) \propto \varepsilon^{7/4}$, where ε is a measure of the anisotropy strength.

In recent years further progress has been made towards understanding solidification phenomena [12] by the advent of by phase-field modelling [13, 14, 15, 16, 17]. The basis of the phase-field technique is the definition of a phase variable, $\phi(\boldsymbol{x},t)$, which is continuous over the whole domain Ω occupied by the system, with $\boldsymbol{x}$ being the spatial coordinates within Ω and t being time. The value of ϕ indicates whether the material is solid or liquid. The continuity of ϕ over Ω implies that the interface between the solid and liquid regions is

diffuse, which is one of the central differences between the phase-field formulation of the dendrite growth problem and microscopic solvability. Like solvability theory, phase-field techniques predict that dendrites will only be formed in the presence of a non-zero crystalline anisotropy [17], and that where dendrites are formed, the tip radius, ρ, is determined by the strength of the anisotropy, ε. The application of phase-field modelling has largely been restricted to two limiting cases: namely the thermally controlled growth of pure substances, and the solidification of relatively concentrated alloys where the solidification is sufficiently slow that the problem may be considered isothermal. This omits two important classes of alloy solidification problems where the isothermal approximation is not valid: the solidification of very dilute alloys, and rapid solidification, where high undercoolings or large thermal gradients drive the solidification at a sufficient rate that the isothermal approximation breaks down.

To date, relatively few attempts have been made to use phase-field techniques to simulate coupled thermo-solutal solidification. The nature of the phase-field model leads to coupled systems of highly non-linear and unsteady partial differential equations which consist of a non-linear phase equation to simulate the microstructure and two diffusion equations to describe the temperature and concentration fields in the model. Moreover, if realistic materials properties are adopted, the ratio of the thermal diffusivity to the solute diffusivity (the Lewis number, $Le = \alpha/D$) is typically 10^3–10^4, leading to severe multiscale problems.

Two basic formulations of the coupled phase-field problem have been reported to date. The first, which has been reported by Loginova et al. [18], follows on from the derivation of the solutal model of Warren and Boettinger [19]. However, there are doubts about the quantitative validity of this model [20] as the numerical results appear to have an unresolved interface width dependence. Moreover, the solute trapping effect reported in this model appears anomalously high. The numerical techniques used to solve this model have

subsequently been improved by Lan et al. [21], who have introduced an adaptive finite volume solver, which allowed them to introduce realistic values of *Le* without the domain boundary effects that had been encountered in Ref. [18]. However, this did not overcome either the excess solute trapping or the interface-width dependence of the solution. An alternative formulation of the coupled phase-field problem has been presented by Ramirez and Beckermann [20, 22], based on the thin interface model developed by Karma [23], although computational limitations meant that this work studied only a restricted set of Lewis numbers, $Le \leq 200$. However, as the thin interface model has been shown to be independent of the length scale chosen for the mesoscopic diffuse interface width, it is capable of giving quantitatively correct predictions for dendritic growth, and consequently this is the model adopted here.

The objective of this work is to apply phase-field modelling to moderately undercooled melts where the dendritic growth is under coupled thermo-solutal control. To date, this has largely only been studied via analytical models such as LGK/LKT, although the omission of crystalline anisotropy means that these models cannot give quantitative predictions for ρ without σ^* being fixed externally. One of the major predictions of the LGK/LKT theory in the deeply undercooled regime is that as the dendritic growth passes from being predominantly solute controlled at high solute Peclet number to being thermally controlled at low thermal Peclet number the dendrite tip radius passes through a local minimum. At yet higher undercooling the dendrite tip radius should pass through a local maximum, whereafter it will decrease smoothly in the regime characterized by a high thermal Peclet number. The effect of undercooling on dendrite tip radius has been investigated in Ref. [20], although they did not find a minimum in ρ, possibly because of the relatively low *Le* of 40 used in their simulations. They did, however, find that despite σ^* tending to approximately the same

limiting value for both pure thermal and pure solutal growth, significant variations in σ* were observed in the coupled thermo-solutal regime.

In this paper we use a coupled thermo-solutal phase-field model of the type presented in Ref. [22] to study the behaviour of V, ρ and σ* for a dendrite growing in a dilute binary alloy as the undercooling is increased. These will be compared with the predictions of the LGK/LKT theories for a dendrite growing at constant σ*, and a brief résumé of the LGK/LKT theory is therefore presented next.

2. Analytical dendrite growth theories

The interfacial undercooling of a parabolic dendritic plate growing into its parent melt undercooled ΔT below its equilibrium liquidus can be written:

$$\Delta T = \Delta T_t + \Delta T_c + \Delta T_r , \tag{3}$$

where ΔT_t, ΔT_c and ΔT_r are the thermal, constitutional and curvature contributions to the undercooling, respectively. ΔT_t is given in two dimensions by [24]:

$$\Delta T_t = -\Delta T_{hyp} \sqrt{\pi Pt}\, \exp(Pt)\, \mathrm{erfc}(\sqrt{Pt}) = \Delta T_{hyp}\, Iv(Pt) , \tag{4}$$

where $\Delta T_{hyp} = L/c_p$ is the hypercooling limit, L is the latent heat on fusion, c_p is the heat capacity at constant pressure, erfc is the complimentary error function and $Iv(Pt)$ is the two-dimensional Ivantsov function.

In a manner analogous to the solution for thermal transport during directional solidification, the solution for solute diffusion leads to isoconcentrate lines that are parabolas of revolution concentric with the freezing front. This leads to an expression for ΔT_c of:

$$\Delta T_c = |m| c_\infty \left(\frac{1}{1-(1-k_E)\Delta c} - 1 \right), \tag{5}$$

where $|m|$ is the slope of the liquidus, k the partition coefficient, defined such that $m(1-k) < 0$, c_∞ the concentration of the alloy in the far field, $\Delta c = Iv(Pc)$, Pc is the solutal Peclet number:

$$Pc = \frac{V\rho}{2D} = Le.Pt\,, \tag{6}$$

D is the diffusion coefficient for the solute species in the liquid, and $Le = \alpha/D$ is the Lewis number. At very low growth velocity, k may be associated with k_E, the equilibrium partition coefficient. However, as the growth velocity increases, we need to take account of solute trapping by writing a velocity-dependent partition coefficient [25]:

$$k(V) = \frac{k_E + aV/\mathrm{D}}{1 + aV/\mathrm{D}}\,. \tag{7}$$

ΔT_r is a manifestation of the Gibbs–Thomson effect, whereby the melting point of a substance on a curved interface is depressed relative to its value on a flat interface by an amount:

$$\Delta T_r = \Gamma K = \frac{2\Gamma}{R} \tag{8}$$

where K is the surface curvature and Γ is the Gibbs–Thomson parameter, given by:

$$\Gamma = \frac{\gamma T_l}{L}\,, \tag{9}$$

where T_l is the equilibrium liquidus temperature and γ the interfacial energy between the solid and liquid phases.

As described above it is assumed that ρ is selected on the basis of a marginal stability criterion, i.e. the dendrite tip grows at the smallest radius that is stable against the growth of small perturbations. The wavelength of these perturbations, and hence the radius of the tip, is given by LGK/LKT, for growth at arbitrary Peclet number, as:

$$\rho = \frac{d_0}{\sigma^* \left[\xi_{\mathrm{T}} Pt + 2\xi_c Pc \frac{|m|c_\infty}{\Delta T_{hyp}} \left(\frac{1-k_E}{1-(1-k_E)\Delta c} \right) \right]}, \tag{10}$$

where in the LGK [5, 6] theory ξ_{T} and ξ_{c} are simply 1, while in the LKT [7] theory these are given by:

$$\xi_{\mathrm{T}} = 1 - \frac{1}{\sqrt{1 + \frac{1}{\sigma^* Pt^2}}} \tag{11}$$

$$\xi_c = 1 + \frac{2k_E}{1 - 2k_E - \sqrt{1 + \frac{1}{\sigma^* Pc^2}}} \quad . \tag{12}$$

3. Phase-field model

The phase-field model adopted here is based upon the coupled thermo-solutal model for the simulation of solidification in dilute binary alloys developed in Ref. [22]. Within this model the phase of the material is represented by the phase variable, ϕ, where the solid and liquid phases correspond to $\phi = 1$ and $\phi = -1$, respectively, and in the interface region ϕ varies smoothly between the bulk values. In the limit of vanishing kinetics the dimensionless governing equations, when expanded [26] into the form used in the numerical implementation presented below, are given by:

$$A^2(\psi)\left[\frac{1}{Le} + Mc_\infty\left[1 + (1-k_E)U\right]\right]\frac{\partial \phi}{\partial t} = 2A(\psi)A'(\psi)\left[\frac{\partial \psi}{\partial x}\frac{\partial \phi}{\partial x} + \frac{\partial \psi}{\partial y}\frac{\partial \phi}{\partial y}\right] + A^2(\psi)\nabla^2\phi$$
$$+ \phi(1-\phi^2) - \lambda(1-\phi^2)^2(\theta + Mc_\infty U) - \frac{\partial}{\partial x}\left(A(\psi)A'(\psi)\frac{\partial \phi}{\partial y}\right) + \frac{\partial}{\partial y}\left(A(\psi)A'(\psi)\frac{\partial \phi}{\partial x}\right)$$

(13)

$$\left(\frac{1+k_E}{2}-\frac{1-k_E}{2}\phi\right)\frac{\partial U}{\partial t}=D\left(-\frac{1}{2}\left[\frac{\partial\phi}{\partial x}\frac{\partial U}{\partial x}+\frac{\partial\phi}{\partial y}\frac{\partial U}{\partial y}\right]+\frac{1-\phi}{2}\nabla^2 U\right)+$$
$$\frac{1}{2\sqrt{2}}\left(\begin{array}{l}\left|1+(1-k_E)U\right|\left(\frac{\partial}{\partial x}\left(\frac{\partial\phi}{\partial t}\frac{\phi_x}{|\nabla\phi|}\right)+\frac{\partial}{\partial y}\left(\frac{\partial\phi}{\partial t}\frac{\phi_y}{|\nabla\phi|}\right)\right)+\\(1-k_E)\left(\frac{\partial U}{\partial x}\left(\frac{\partial\phi}{\partial t}\frac{\phi_x}{|\nabla\phi|}\right)+\frac{\partial U}{\partial y}\left(\frac{\partial\phi}{\partial t}\frac{\phi_y}{|\nabla\phi|}\right)\right)\end{array}\right)+$$
$$\frac{1}{2}\left(\left|1+(1-k_E)U\right|\frac{\partial\phi}{\partial t}\right)$$

(14)

$$\frac{\partial\theta}{\partial t}=\alpha\nabla^2\theta+\frac{1}{2}\frac{\partial\phi}{\partial t}$$

(15)

where ψ = arctan(ϕ_x/ϕ_y) is the angle between the normal to the interface and the *x*-axis, and $A(\psi) = 1 + \varepsilon.\cos(\eta\psi)$ is an anisotropy function with strength ε and mode number η. The dimensionless coupling parameter, λ, is given by Ref. [23] as:

$$\lambda=\frac{D}{a_2}=\frac{a_1 W_0}{d_0}, \qquad (16)$$

where d_0 is the chemical capillary length. In order to simulate kinetic free growth it is shown in Ref. [23] that a_1 and a_2 take the values $5\sqrt{2}/8$ and 0.6267 respectively. Here the solutal and thermal diffusivities have now both been non-dimensionalized by multiplying by $\tau_0/{W_0}^2$, where τ_0 is a characteristic relaxation time given by:

$$\tau_0=\frac{d_0^2 a_2\lambda^3}{D a_1^2},$$

(17)

and $W_0 = d_0\lambda/a_1$ is a measure of the width of the diffuse interface.

The dimensionless concentration and temperature fields U and θ are related to their physical counterparts c and T via the relations:

$$U = \frac{1}{1-k_E}\left(\left(\frac{2c/c_\infty}{1+k_E-(1-k_E)\phi}\right)-1\right)$$

(18)

and

$$\theta = \frac{\Delta T - mc_\infty}{L/c_p}.$$

(19)

Finally, the dimensionless gradient of the liquidus line, M, is given by:

$$M = \frac{|m|(1-k_E)}{L/c_p}.$$

(20)

4. Numerical methods

The nature of the phase-field method, where rapid changes in the phase variable, ϕ, are restricted to a narrow interface region, lends itself naturally to adaptive mesh refinement. Here we discretize the governing equations using a finite difference approximation based upon a quadrilateral, non-uniform, refined mesh with equal grid spacing in both directions at each level of refinement, which allows the application of standard finite difference stencils.

The mesh structure adopted is non-conforming, in the sense that we allow hanging nodes [27]. We distinguish between four different node types: internal nodes, boundary nodes, hanging nodes and interface nodes. In the case of a uniformly refined mesh, all nodes are either internal nodes or boundary nodes. In the case of non-uniformly refined meshes, the nodes that lie at the interface of two levels of refinement are termed as either interface nodes or hanging nodes. Hanging nodes are nodes that exist only on the finer grids, while interface

nodes exist on both the finer and next coarser grid (see Fig. 1). Standard second-order central difference schemes are used to approximate the first and second differentials of ϕ, U and θ, while a compact nine-point scheme has been used for the Laplacian terms in the phase equation as this has been shown to reduce mesh-induced anisotropy effects [28, 29]. The mesh data is stored in a quadtree data structure as in Ref. [30].

In order to ensure that sufficient levels of refinement occur around the interface region and that the extreme multiscale nature of the thermal and solutal diffusion fields at high Lewis numbers are handled appropriately, adaptive refinement is based upon an elementwise gradient criterion given by:

$$E = h_{|\nu|}\left(|\nabla\phi| + E_C|\nabla U| + E_T|\nabla\theta|\right),$$

(21)

where $h_{|\nu|}$ is the element size on the finest level of refinement, and E_C and E_T are user-defined constants which control the respective effect of the concentration and thermal fields relative to the phase-field. These are compared to two tolerances, E_{Tol}^{+} and E_{Tol}^{-}. If, at any location within the domain $E \geq E_{Tol}^{+}$, the mesh is refined at that location, while conversely if $E \leq E_{Tol}^{-}$ the mesh is permitted to coarsen at that location. Refinement and coarsening proceeds via a two-step process. On the first sweep through the mesh the elements targeted for refinement (coarsening) based upon the gradient criterion are marked, and on the second sweep the marked elements are refined/coarsened. In order to guarantee that the solution is sufficiently resolved, a number, N_s, of extra (safety) layers of elements may be added to those marked by the gradient criterion at each level. This helps to ensure that the interface region does not move out of the most refined area of the mesh during a given time-step. In addition we apply two further refinement rules:

- Two neighbouring elements should differ by at most one level of refinement.

- An element cannot be further refined once it has reached a user-defined maximum level of refinement.

The most commonly employed temporal discretization schemes utilized in phase-field modelling are explicit methods such as the forward Euler scheme. Rewriting Eqs. (13)-(15) in operator form:

$$\frac{\partial \phi}{\partial t} = F_\phi(t,\phi,U,\theta),\ \frac{\partial U}{\partial t} = F_U\left(t,U,\phi,\frac{\partial \phi}{\partial t}\right),\ \frac{\partial \theta}{\partial t} = F_\theta\left(t,\theta,\frac{\partial \phi}{\partial t}\right)$$

(22)

the forward Euler scheme can be written as:

$$\begin{bmatrix} \phi^{k+1} \\ U^{k+1} \\ \theta^{k+1} \end{bmatrix} - \begin{bmatrix} \phi^{k} \\ U^{k} \\ \theta^{k} \end{bmatrix} = \Delta t \begin{bmatrix} F_\phi\left(t^k,\phi^k,U^k,\theta^k\right) \\ F_U\left(t^k,U^k,\phi^k,\dot{\phi}^{k+1}\right) \\ F_\theta\left(t^k,\theta^k,\dot{\phi}^{k+1}\right) \end{bmatrix}.$$

(23)

The implementation of explicit methods is straightforward, but they suffer from a time-step restriction in order to ensure the stability of the discretization scheme, which is of the form:

$$\Delta t \le C.h^2,$$

(24)

where h is the minimum element size and for some non-linear partial differential equations the value of C can be very small, leading to excessively small time steps on heavily refined grids. Moreover, we have shown elsewhere [26] that for the complex equations considered here $C = C(\lambda, Le, \Delta)$, with C varying from ~0.3 at Le = 1 to $C \le 0.001$ at Le = 500 at which point the tests to evaluate to C were terminated due to the extremely long computational time required to evaluate the explicit Euler method, despite Le = 500 still being significantly short of values typical of liquid metals.

In order to overcome these restrictions, implicit time-stepping methods have been utilized here as these may be designed to be unconditionally stable. In particular, we have used the second-order backward difference formula (BDF2), which is an implicit linear two-step method, which, with a constant time step, Δt, takes the following form:

$$\frac{3}{2}\begin{bmatrix}\phi^{k+1}\\ U^{k+1}\\ \theta^{k+1}\end{bmatrix}-2\begin{bmatrix}\phi^{k}\\ U^{k}\\ \theta^{k}\end{bmatrix}+\frac{1}{2}\begin{bmatrix}\phi^{k-1}\\ U^{k-1}\\ \theta^{k-1}\end{bmatrix}=\Delta t\begin{bmatrix}F_{\phi}\left(t^{k+1},\phi^{k+1},U^{k+1},\theta^{k+1}\right)\\ F_{U}\left(t^{k+1},U^{k+1},\phi^{k+1},\dot{\phi}^{k+1}\right)\\ F_{\theta}\left(t^{k+1},\theta^{k+1},\dot{\phi}^{k+1}\right)\end{bmatrix}. \quad (25)$$

The method leads to second-order convergence in both time and space. It can be shown that the BDF2 method is A-stable [31], and is therefore used for stiff systems of differential equations. The advantage over one-step second-order methods such as Crank–Nicholson is that only one non-linear solution is required at each time-step. The (small) price that has to be paid for this computational efficiency is that the solutions from the previous two time-steps must be saved. Although highly dependent upon the problem, particularly the value of *Le*, convergence studies [26] have shown that the BDF2 method permits time steps between 80 and several hundred times that allowed by the explicit forward Euler method.

Utilizing an implicit time discretization scheme, the appropriate selection of Δt shifts from being a question of numerical stability to one of accuracy. For typical phase-field simulations, growth starts from a small nucleus. The initial growth of the nucleus will typically be very rapid, although the inherent instability of the interface will lead to the formation of dendritic arms that will ultimately grow with a steady-state velocity. Consequently, an adaption of the time step in the BDF2 method is likely to be efficient and lead to an adaptive time and space discretization method. It can be shown that in order to ensure second-order convergence with a variable time step of ratio, $r = \Delta t_k/\Delta t_{k-1}$, Eq. (25) becomes:

$$\frac{1+2r}{1+r}\begin{bmatrix}\phi^{k+1}\\ U^{k+1}\\ \theta^{k+1}\end{bmatrix}-(r+1)\begin{bmatrix}\phi^{k}\\ U^{k}\\ \theta^{k}\end{bmatrix}+\frac{r^2}{1+r}\begin{bmatrix}\phi^{k-1}\\ U^{k-1}\\ \theta^{k-1}\end{bmatrix}=\Delta t\begin{bmatrix}F_\phi\left(t^{k+1},\phi^{k+1},U^{k+1},\theta^{k+1}\right)\\ F_U\left(t^{k+1},U^{k+1},\phi^{k+1},\dot{\phi}^{k+1}\right)\\ F_\theta\left(t^{k+1},\theta^{k+1},\dot{\phi}^{k+1}\right)\end{bmatrix}.$$

(26)

The choice of appropriate time steps is based upon a set of local error estimators:

$$D_k^{\phi}=\frac{r}{r+1}\left\|\phi^{k+1}-(1+r)\phi^{k}+r\phi^{k-1}\right\|_{\infty}$$

(27)

$$D_k^{U}=\frac{r}{r+1}\left\|U^{k+1}-(1+r)U^{k}+rU^{k-1}\right\|_{\infty}$$

(28)

$$D_k^{\theta}=\frac{r}{r+1}\left\|\theta^{k+1}-(1+r)\theta^{k}+r\theta^{k-1}\right\|_{\infty}$$

(29)

Each of the error estimators is compared against a corresponding tolerance ($D_{Tol}^{\phi}, D_{Tol}^{U}, D_{Tol}^{\theta}$) and if at any time-step the local temporal error $D_k = \min(D_{Tol}^{\phi}, D_{Tol}^{U}, D_{Tol}^{\theta}) \le D_{Tol}$ the time step is accepted and the next time-step is increased, whereas if $D_k \ge D_{Tol}$ the step is rejected and retaken with a smaller time-step. The rate at which the time-step should grow can be estimated from:

$$r=\left(\frac{D_{Tol}}{D_k}\right)^{\frac{1}{1+p}},$$

(30)

where *p* is the order of the scheme, which is 2 for the BDF2 method.

When using implicit time discretization methods it is necessary to solve a system of non-linear algebraic equations at each time-step. Multigrid methods are among the fastest

available solvers for large sparse systems of linear equations and in this work we apply the non-linear generalization known as FAS directly to the algebraic system that arises at each time-step. This is the key ingredient that allows the practical implementation of implicit time stepping and is based upon two principles: the coarse grid principle and the smoothing principle. For the coarse grid correction one has to define grid transfer operators to transfer the solution and the residual from the fine grid to the coarse grid and the solution from the coarse to the fine grid. Here, bilinear interpolation is used for the coarse to fine grid transfer and injection is used for the fine to coarse transfer. For smoothing the error we use a basic pointwise nonlinear weighted Gauss–Seidel method, with:

$$\phi_{ij}^{k+1} = \phi_{ij}^{k+1} - \omega \frac{\left(F_{\phi}^{*}\left(\phi^{k+1}, U^{k+1}, \theta^{k+1}\right)_{ij} - \left((r+1)\phi_{ij}^{k} - \frac{r^2}{1+r}\phi_{ij}^{k-1} \right) \right)}{\frac{\partial}{\partial \phi_{ij}} F_{\phi}^{*}\left(\phi^{k+1}, U^{k+1}, \theta^{k+1}\right)_{ij}}$$

(31)

$$U_{ij}^{k+1} = U_{ij}^{k+1} - \omega \frac{\left(F_{U}^{*}\left(U^{k+1}, \phi^{k+1}, \dot{\phi}^{k+1}\right)_{ij} - \left((r+1)U_{ij}^{k} - \frac{r^2}{1+r}U_{ij}^{k-1} \right) \right)}{\frac{\partial}{\partial \phi_{ij}} F_{U}^{*}\left(U^{k+1}, \phi^{k+1}, \dot{\phi}^{k+1}\right)_{ij}}$$

(32)

$$\theta_{ij}^{k+1} = \theta_{ij}^{k+1} - \omega \frac{\left(F_{\theta}^{*}\left(\theta^{k+1}, \phi^{k+1}, \dot{\phi}^{k+1}\right)_{ij} - \left((r+1)\theta_{ij}^{k} - \frac{r^2}{1+r}\theta_{ij}^{k-1} \right) \right)}{\frac{\partial}{\partial \phi_{ij}} F_{\theta}^{*}\left(\theta^{k+1}, \phi^{k+1}, \dot{\phi}^{k+1}\right)_{ij}}$$

(33)

with

$$F_{\phi}^{*}\left(\phi^{k+1}, U^{k+1}, \theta^{k+1}\right) = -\Delta t F_{\phi}\left(t^{k+1}, \phi^{k+1}, U^{k+1}, \theta^{k+1}\right) + \frac{1+2r}{1+r}\phi^{k+1}$$

(34)

$$F_U^*\left(U^{k+1},\phi^{k+1},\dot{\phi}^{k+1}\right)=-\Delta t F_U\left(t^{k+1},U^{k+1},\phi^{k+1},\dot{\phi}^{k+1}\right)+\frac{1+2r}{1+r}U^{k+1}$$

(35)

$$F_\theta^*\left(\theta^{k+1},\phi^{k+1},\dot{\phi}^{k+1}\right)=-\Delta t F_\theta\left(t^{k+1},\theta^{k+1},\dot{\phi}^{k+1}\right)+\frac{1+2r}{1+r}\theta^{k+1}$$

(36)

where the evaluation of the derivatives of the discretization operators with respect to the system variable is discussed in Ref. [26].

On the basis of the described smoothing and transfer operators a multigrid solver for adaptively refined meshes has been developed based on the full approximation scheme (FAS) [27] for resolving the non-linearity. The number of pre- and post-smoothing operations required for optimal convergence has been investigated within the context of phase-field simulation in Refs. [26, 32]. Based on that work we have used a V-cycle iteration with two pre- and two post-smoothing operations.

A major property of the multigrid method is *h*-independent convergence, which means that the convergence rate does not depend on the element size. This behaviour is vital in respect of being able to solve the extreme multiscale problem arising from coupled thermo-solutal phase-field simulations at high Lewis numbers.

5. Calculation of the dendrite tip velocity and radius of curvature

The two most important parameters to come out of quantitative phase-field simulations are the curvature and velocity of the dendrite tip, which therefore need to be calculated with a high degree of accuracy. The calculation of both these quantities requires accurate estimation of the tip position, for which we use a high-order inverse interpolation scheme.

For a dendrite arm growing along the x-axis, which consists of the discrete points x_j, for $j = 1,N$, we are seeking the value x^* on the x-axis, for which $\phi(x^*) = 0$. The method adopted here is based on Newton forward differences, wherein:

$$x^* = x_j + \vartheta_i \left(x_{j+1} - x_j \right),$$

(37)

where i is the order of the interpolation and

$$\vartheta_1 = \frac{1}{\Delta\phi_j} \left(\phi(x^*) - \phi(x_j) \right)$$

(38)

$$\vartheta_2 = \frac{1}{\Delta\phi_j} \left(\phi(x^*) - \phi(x_j) - \frac{\vartheta_1(\vartheta_1 - 1)}{2} \Delta^2\phi_j \right)$$

(39)

$$\vartheta_3 = \frac{1}{\Delta\phi_j} \left(\phi(x^*) - \phi(x_j) - \frac{\vartheta_1(\vartheta_1 - 1)}{2} \Delta^2\phi_j - \frac{\vartheta_2(\vartheta_2 - 1)(\vartheta_2 - 2)}{6} \Delta^3\phi_j \right)$$

(40)

$$\vartheta_4 = \frac{1}{\Delta\phi_j} \left(\begin{array}{l} \phi(x^*) - \phi(x_j) - \frac{\vartheta_1(\vartheta_1 - 1)}{2} \Delta^2\phi_j - \frac{\vartheta_2(\vartheta_2 - 1)(\vartheta_2 - 2)}{6} \Delta^3\phi_j \\ - \frac{\vartheta_3(\vartheta_3 - 1)(\vartheta_3 - 2)(\vartheta_3 - 3)}{24} \Delta^4\phi_j \end{array} \right)$$

(41)

where $\phi(x^*) = 0$ in this case and

$$\Delta\phi_j = \phi_{j+1} - \phi_j$$

(42)

$$\Delta^2\phi_j = \Delta\phi_{j+1} - \Delta\phi_j = \phi_{j+2} - 2\phi_{j+1} + \phi_j$$

(43)

$$\Delta^3\phi_j = \Delta^2\phi_{j+1} - \Delta^2\phi_j = \phi_{j+3} - 3\phi_{j+2} + 3\phi_{j+1} - \phi_j$$

(44)

$$\Delta^4\phi_j = \Delta^3\phi_{j+1} - \Delta^3\phi_j = \phi_{j+4} - 4\phi_{j+3} + 6\phi_{j+2} - 4\phi_{j+1} + \phi_j .$$

(45)

With a relatively exact calculation of the position of the interface we can now compute the curvature of the tip:

$$K = \frac{\partial^2 x / \partial y^2}{\left(1 + (\partial x / \partial y)^2\right)^{3/2}}$$

(46)

and hence the actual radius of curvature at the tip:

$$\rho_a = \frac{1}{|K|} .$$

(47)

However, the actual tip radius is often not suitable for comparison with theoretical results [20, 28, 33], as most dendrite growth theories assume a parabolic tip shape. Therefore, the procedure from Ref. [20] is adopted for calculating the parabolic tip radius. We introduce a local Cartesian coordinate system (x, y), situated at the actual tip position where x is pointing along the growth direction. The form of the parabola is then described by:

$$y^2 = -2\rho(x - x_0) ,$$

(48)

where ρ is the parabolic tip radius and x_0 is the effective tip location. A simple least-squares fit to the $\phi = 0$ isoline is used to determine the optimum values for ρ and x_0, which is applied over a fitting range:

$$\tilde{x} = \left| x_{\text{left}}, x_{\text{right}} \right|. \qquad (49)$$

6. Results

The phase-field model used here is formally identical to that derived in Ref. [22], where the ability of the model to yield quantitative predictions is extensively validated. For this reason we do not repeat the validation of the model derivation. We give below the results of some comparative simulations which were also run in Refs. [20, 22] which we use to confirm that the numerical implementation of the model described above performs as expected. A far more extensive validation of our numerical techniques is presented in Ref. [26]. Having established the validity of the numerical scheme employed, we then move on to present the results of a set of simulations designed to investigate the selection of the dendrite tip radius and growth velocity as the undercooling is increased. In particular, we examine the regime where the dendrite passes from being predominantly solutally, to thermally, controlled at sufficiently high Lewis number that in so doing a radius minimum is encountered.

The initial numerical validation has been undertaken at a modest Lewis number of 40, for which results have been published in Ref. [20] with which ours may be directly compared. The coupled model described by Eqs. (13)-(15) has been solved for the domain Ω = [-800, 800]^2, with simulation parameters $\Delta = 0.55$, $Mc_\infty = 0.07$, $Le = 40$, $\varepsilon = 0.02$, $k_E = 0.15$. In order to simulate kinetic free growth, Eq. (16) is used with $\lambda = 2$, which leads to D = 1.253328. Since the Lewis number is set to 40 it follows that the thermal diffusivity is $\alpha = 50.13311$. The mesh refinement parameters have been set as $E_C = 0.75$ and $E_T = 1.0$. The problem is solved using a maximum of 11 levels of refinement, giving a minimum h of 0.78. This is equivalent, were a uniform mesh to have been used, of a mesh size which is $2^{11} \times 2^{11}$. The multigrid solver is iterated until an absolute residual of 10^{-5} is reached and the tolerance on the adaptive time-stepping routine, D_{Tol}, is set to 7.5×10^{-3}. A typical mesh structure is

shown in Fig. 2, while characteristic results for the thermal (θ) and solutal fields (c/c_∞) towards the end of the simulation are shown in Fig. 3, where boundary effects are already beginning to affect the simulation results. Even at this rather modest Lewis number it is clearly evident that the thermal field extends much more widely than the solute field. For this simulation the steady-state values of the growth velocity and dendrite tip radius are $\rho_a/d_0 = 16.34$ and $Vd_0/\alpha = 0.0040$. Fitting of a parabolic profile to the $\phi = 0$ isoline, as described by Eq. (48), results in a parabolic radius of curvature $\rho/d_0 = 27.38$, which also gives $V\rho/2\alpha = 0.0546$. The fitting interval here is $\tilde{x} = \left|-100, -10\right|$, although keeping the fitting range constant and moving the fitting interval a further 40 units to the right changes ρ by no more than 1.5%.

We believe that all of these results compare favourably with the results presented by Ramirez and Beckerman [20, Figs. 3 and 4]. Moreover, when the phase equation was solved directly in Ref. [20], using an explicit finite difference scheme, a severe grid dependence was found. This meant that small values of h (typically $h \approx 0.3$) had to be used to get accurate solutions, with no converged solution at all being found for $h > 1$. The problem was overcome by using a preconditioning technique, in which the phase equation was written in terms of a new variable $\psi = \tanh(\phi/\sqrt{2})$. In contrast, using an implicit multigrid solver no such h dependence has been encountered. In numerical tests presented in Ref. [26] the variation in tip velocity was found to vary by no more than 5% as h was reduced from 0.78 to 0.097.

In Ref. [20] another issue of potential concern to the authors was a significant variation between simulations as the coupling parameter, λ, was varied over the range 1-8. The variation in the upper part of this range is probably not a major issue. Eq. (16) gives the length scale W_0 corresponding to $\lambda = 4$ as $4.53d_0$, while for $\lambda = 8$ this is $W_0 = 9.05d_0$, i.e. 28-55% of ρ_a. Given that W_0 is a measure of the width of the diffuse interface, it would not be

surprising if the quality of the solution were to degrade as the width of the diffuse interface approached the actual radius of curvature of the dendrite tip. However, of more concern is the variation observed in the solution as λ is varied in the range 1-4, most notably a ~40% decrease in the tip velocity as λ is decreased. As one of the fundamental properties of the thin-interface model is that the solutions should be independent of the mesoscopic interface width, this an effect that we have chosen to investigate further with the multigrid method reported here. Fig. 4 shows the variation of the scaled velocity Vd_0/α as a function of λ and should be directly comparable to the solid line in Ref. [20, Fig. 5]. Unlike Ref. [20], which reported a variation in Vd_0/α of up to 25% between $\lambda = 1$ and $\lambda = 4$, we observe a much smaller variation of no more than 10% over the same interval. However, the most notable effect is the sharp increase in Vd_0/α for $\lambda < 1$, which corresponds to the width of the diffuse interface being less than the capillary length. Fig. 5, which shows the Peclet number as a function of λ, would tend to confirm that this is a real effect. For $\lambda > 1.5$, *Pt* is remarkably constant, with a mean value of 0.0563 ± 0.0005, but again for small values of λ a strong systematic increase is observed. However, as yet the exact origins for this variation are unknown.

We now move on to consider the variation of ρ as Δ is increased. Fig. 6 shows a family of plots of ρ against Δ calculated using the LKT [7] model. The parameters used here are $Mc_\infty = 0.05$, $k_E = 0.30$ and $\sigma^* = 0.05$. The curves clearly show that the depth of the predicted minimum is a strong function of *Le*, while both the predicted minimum and maximum occur at lower values of Δ as *Le* is increased. It is apparent from Fig. 6 that the minimum value of *Le* at which we might reasonably expect to be able to observe a minimum in ρ is $Le = 200$, which accordingly is the value adopted in the phase-field simulations. The simulations are run on a domain of size $\Omega = [-1600, 1600]^2$, which is larger than the previous set of simulations as the higher Lewis gives rise to a more extensive thermal boundary layer. A maximum of 12

levels of refinement are used, which as before gives a minimum h of 0.78, equivalent, were a uniform mesh to have been used, of a mesh size which is $2^{12} \times 2^{12}$. The other parameters used in the simulation are $\varepsilon = 0.02$ and $\lambda = 1$. This final parameter has been chosen as a compromise between the anomalous behaviour observed in Fig. 4 and the need to keep the ratio of the interface width to the solute boundary layer width (W_0V/D) less than or of the order of unity [20], as this quantity increases rapidly with the high growth velocities encountered at elevated undercoolings. Values for the tip velocity, V, and tip radius, ρ, for a family of simulations run at different values of Δ between 0.1 and 0.8 are shown in Figs. 7 and 8 respectively. The velocity shows a simple power-law dependence on Δ of the form $V \propto \Delta^{\beta}$, which has been widely reported as being the case in experimental velocity-undercooling studies (see e.g. [34, 35]), where β is a material-dependent constant that is typically in the range 2.0-3.5. The least-squares value of β found for the simulations reported here is 2.39. As is apparent from Fig. 8, a clear radius minimum is observed in the data, albeit at a rather higher value of Δ than would have been expected from the LKT theory. There is, however, no evidence of a velocity maximum, despite the fact that from the LKT prediction this should occur well below the maximum Δ studied here of 0.8. Yet higher values of Δ have not been studied as the value of W_0V/D for $\Delta = 0.8$ is 1.6, and although this is probably still acceptable [20], significantly higher values may lead to computational artefacts in the solution.

In order to better understand the observed results, we have calculated σ^* as a function of Δ, using both the LGK and LKT definitions. In both models this would be expected to be a material-dependent constant, although for both pure thermal and pure solutal growth in two dimensions [20] and pure thermal growth in three dimensions [28], σ^* appears to decrease approximately linearly with increasing Peclet number, with the coupled thermo-solutal model of Ref. [20] showing a rather steeper decrease in σ^*. In order to calculate σ^* in such a way

that it is independent of the Ivantsov solution when Δc is evaluated, the following procedure has been adopted from Ref. [20]. Δc can be written as:

$$\Delta c = \frac{U_i}{1+(1-k_E)U_i},$$

(50)

where U_i is the value of U "frozen in" at the interface. (NB: there is an error in Ref. [20] which meant that Eq. (50) appeared as $U_i[1+(1-k_E)Ui]$). The correct form is as shown above, although there is no evidence this is anything other than a typesetting error in Ref. [20], as the results presented are consistent with the correct form of the equation.) U_i may either be read directly from the simulations or evaluated from:

$$U_i = \frac{-d_0(1-15\varepsilon)\rho_a - \theta_i}{Mc_\infty},$$

(51)

where θ_i is the value of θ at the interface. The latter of the two methods has been used here, with θ_i being evaluated at $\phi = 0.9$, although as the solid is essentially isothermal the value obtained does depend critically upon the value of ϕ selected.

The results of calculating the selection parameter, σ^*, are shown in Fig. 9, for both the LGK and LKT approaches. As in Ref. [20], we find that as $Pt \to 0$, σ^* approaches a value of approximately 0.07, which is consistent with it being independent of the alloy concentration in the low undercooling limit (note that although we have used different material parameters, this should not matter as in the limit $Pt \to 0$, and σ^* should depend only upon ε, which is the same as in Ref. [20]). However, unlike Ref. [20] we find at higher Lewis numbers a very significant difference in behaviour between the LGK and LKT definitions of σ^*. On the LGK definition σ^* drops monotonically, reaching at the highest Peclet numbers studied a very low

value, around 0.0006. In fact, above $Pt = 0.15$, σ^* on the LGK definition is very close to varying in direct proportion to $1/Pt$. In contrast, on the LKT definition, σ^* varies non-monotonically, showing a minimum at $Pt = 0.0325$ ($\Delta = 0.4$), coincident with the minimum in ρ, while the maximum in σ^* occurs at $\Delta = 0.65$ ($Pt = 0.14$), an undercooling that does not correspond to any obvious feature in the plot of ρ against Δ.

However, the physical significance of these results is far from clear. One would have expected a priori the LKT definition of σ^* to be superior due to the high undercooling corrections effected by the inclusion of the terms ξ_T and ξ_c. Indeed, the inclusion of the ξ parameters keeps σ^* (on the LKT definition) constant to within a factor of ~2, while on the LGK definition σ^* varies by over two orders of magnitude. The variation of the ξ parameters with Pt is shown in Fig. 10, showing in particular that across the range of undercoolings studied here, ξ_c varies from close to 1 (solute dominated growth) to essentially 0 (no solute effects). However, from a quantitative point of view a variation by a factor of 2 is still significant, particularly when it is borne in mind that in the most widely used method for estimating the characteristic microstructural length scale for rapid solidification processes is still the use of the LKT model with a constant σ^* estimated from the anisotropy in the zero Peclet number limit.

7. Summary and Discussion

A model has been presented which allows the efficient numerical solution of the non-isothermal phase-field equations for alloy solidification using advanced numerical techniques such as mesh adaptivity, implicit time-stepping and multigrid methods. Moreover, by using a formulation of the non-isothermal problem based on the thin-interface model these results should be independent of the width assumed for the diffuse interface, giving them a quantitative validity that cannot be claimed by other formulations of the non-isothermal

problem. We have used this model to investigate the behaviour of the dendrite tip radius and growth velocity as a function of undercooling for a dilute alloy at a Lewis number of 200, confirming theoretically for the first time that the dendrite tip radius does indeed pass through a minimum with increasing undercooling. However, up to the highest undercooling studied ($\Delta = 0.8$) no evidence of a radius maximum has been observed. The radius selection parameter, σ^*, has been calculated as a function of undercooling and this is shown to be far from being constant, with approximately a factor of 2 variation observed (LKT definition of σ^*) over the range of undercoolings studied. This highlights the potential limitations of assuming constant σ^* in simple analytical models of solidification to predict dendrite length scales.

References

[1] Corrigan DP, Koss MB, LaCombe JC, et al. Phys. Rev. E 1999; 60:7217.

[2] Bisang U, Bilgram JH. Phys. Rev. E 1996 54:5309.

[3] Ivantsov GP. Doklady Akademii Nauk SSSR 1947; 58:567.

[4] Mullins WW, Sekerka RF. J. Appl. Phys. 1964; 33:444.

[5] Lipton J, Glicksman ME, Kurz W. Mater. Sci. Eng. 1984; 65:57.

[6] Lipton J, Glicksman ME, Kurz W. Metall. Trans. A 1987; 18:341.

[7] Lipton J, Kurz W, Trivedi R. Acta metall. 1987; 35:957.

[8] Willnecker R, Herlach DM, Feuerbacher B. Phys. Rev. Lett. 1989; 62:2707.

[9] Huang SC, Glicksman ME. Acta metall. 1981; 29:701.

[10] Kessler DA, Koplik J, Levine H. Adv. Phys. 1988; 37:255.

[11] Pomeau Y, Ben-Amar M. In: Solids far from equilibrium, Cambridge University Press, 1992. p. 365.

[12] Mullis AM, Cochrane RF. Acta mater. 2001; 49:2205.

[13] Langer JS. In: Grinstein G & Mazenko G, editors. Directions in condensed matter physics, World Science 1986. p. 164.

[14] Caginalp G. Phys. Rev. A 1989; 39:5887.

[15] Penrose O, Fife PC. Physica D 1990 43:44.

[16] Kobayashi R. Physica D 1993; 63:410.

[17] Wheeler AA, Murray BT, Schaefer RJ. Physica D 1993; 66:243.

[18] Loginova I, Amberg G, Aagren J. Acta mater. 2001; 49:573.

[19] Warren JA, Boettinger WJ. Acta metall. mater. 1995; 43:689.

[20] Ramirez JC, Beckermann C. Acta mater. 2005; 53:1721.

[21] Lan CW, Chang YC, Shih CJ. Acta mater. 2003; 51:1857.

[22] Ramirez JC, Beckermann C.. Phys. Rev. E 2004; 69:051607.

[23] Karma A. Phys. Rev. Lett. 2001; 87:115701.

[24] Horvay G, Cahn JW. Acta metall. 1961; 9:695.

[25] Aziz MJ. J. Appl. Phys. 1982; 53:1158.

[26] Rosam J. A fully implicit, fully adaptive multigrid method for multi-scale phase-field modelling, Ph.D. thesis, University of Leeds, 2007.

[27] Trottenberg U, Oosterlee C, Schüller A. Multigrid, Academic Press, 2001.

[28] Karma A, Rappel WJ. Phys. Rev. E 1998; 57:4323.

[29] Echebarria B, Folch R, Karma A, Plapp M. Phys. Rev. E 2004; 70:061604.

[30] Provatas N, Goldenfeld N, Dantzig J. J. Comp. Phys. 1999; 148:265.

[31] W. Hundsorfer, J.G. Verwer. Numerical Solution of Time-Dependant Advection-Diffusion-Reaction Equations, Springer-Verlag, 2003.

[32] Rosam J, Jimack PK, Mullis AM. J. Comp. Phys. 2007; 225:1271.

[33] Tong X, Beckermann, C, Karma A, Q. Li. Phys. Rev. E 2001; 63:R49.

[34] Eckler K, Herlach DM. Mater. Sci. Eng. A 1994; 128:159.

[35] Dragnevski KI, Cochrane RF, Mullis AM. Metall. Mater. Trans. A 2004; 35:3211.

Figure Captions

Fig. 1. Schematic illustration of the different node types occurring in an adaptively refined mesh. • interior nodes, Y boundary nodes, % hanging nodes and o interface nodes.

Fig. 2. Typical mesh structure for a dendrite growing on a mesh with a maximum of 11 levels of refinement.

Fig. 3. Thermal and solutal fields around a dendrite growing with a Lewis number of 40 (the solid–liquid interface has been outlined on the thermal map for clarity).

Fig. 4. Variation of the dimensionless dendrite growth velocity as a function of the coupling parameter, λ. Note large variation for $\lambda < 1$.

Fig. 5. Variation of the Peclet number as a function of the coupling parameter, λ.

Fig. 6. Dendrite tip radius as a function of undercooling for Lewis numbers in the range 50-1000 as calculated using the LKT model for alloy solidification.

Fig. 7. Dimensionless dendrite growth velocity as a function of undercooling, showing very close agreement to a simple power-law dependence.

Fig. 8. Dimensionless dendrite tip radius as a function of undercooling, showing a clear minimum at a dimensionless undercooling of 0.4.

Fig. 9. Radius selection parameter calculated on (a) the LGK (no high undercooling corrections) and (b) the LKT (corrected for high undercooling) basis. In both cases the value in the limit $Pt \rightarrow 0$ tends to 0.07, which is consistent with analytical solutions for an anisotropy strength of 0.02.

Fig. 10. Values of the thermal and solutal correction parameters (ξ_t and ξ_c) used in the LKT calculation of the radius selection parameters, σ^*.

Figure 01, TIFF, LZW cmpress
Click here to download high resolution image

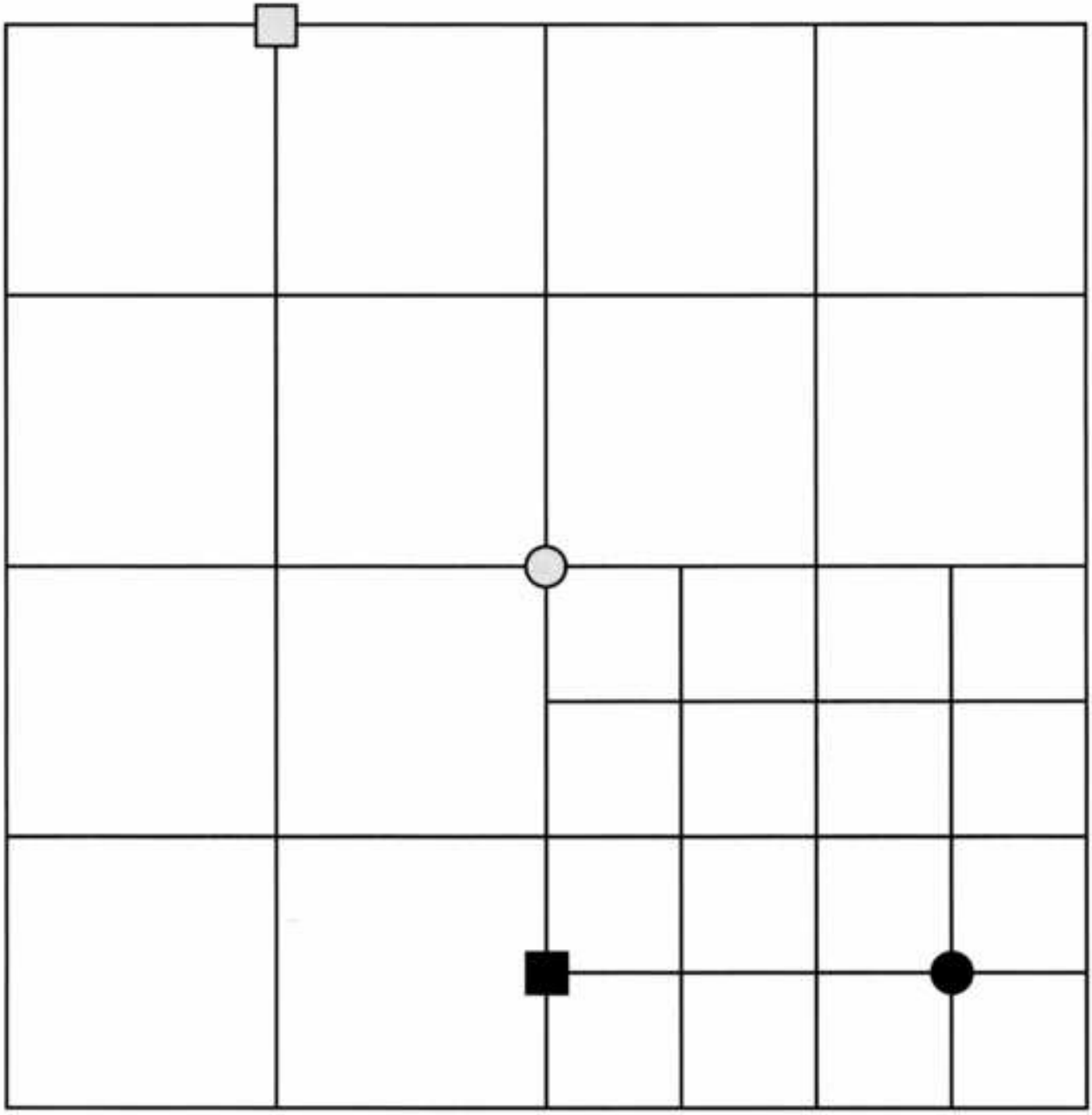

Figure 02, TIFF, LZW cmpress
Click here to download high resolution image

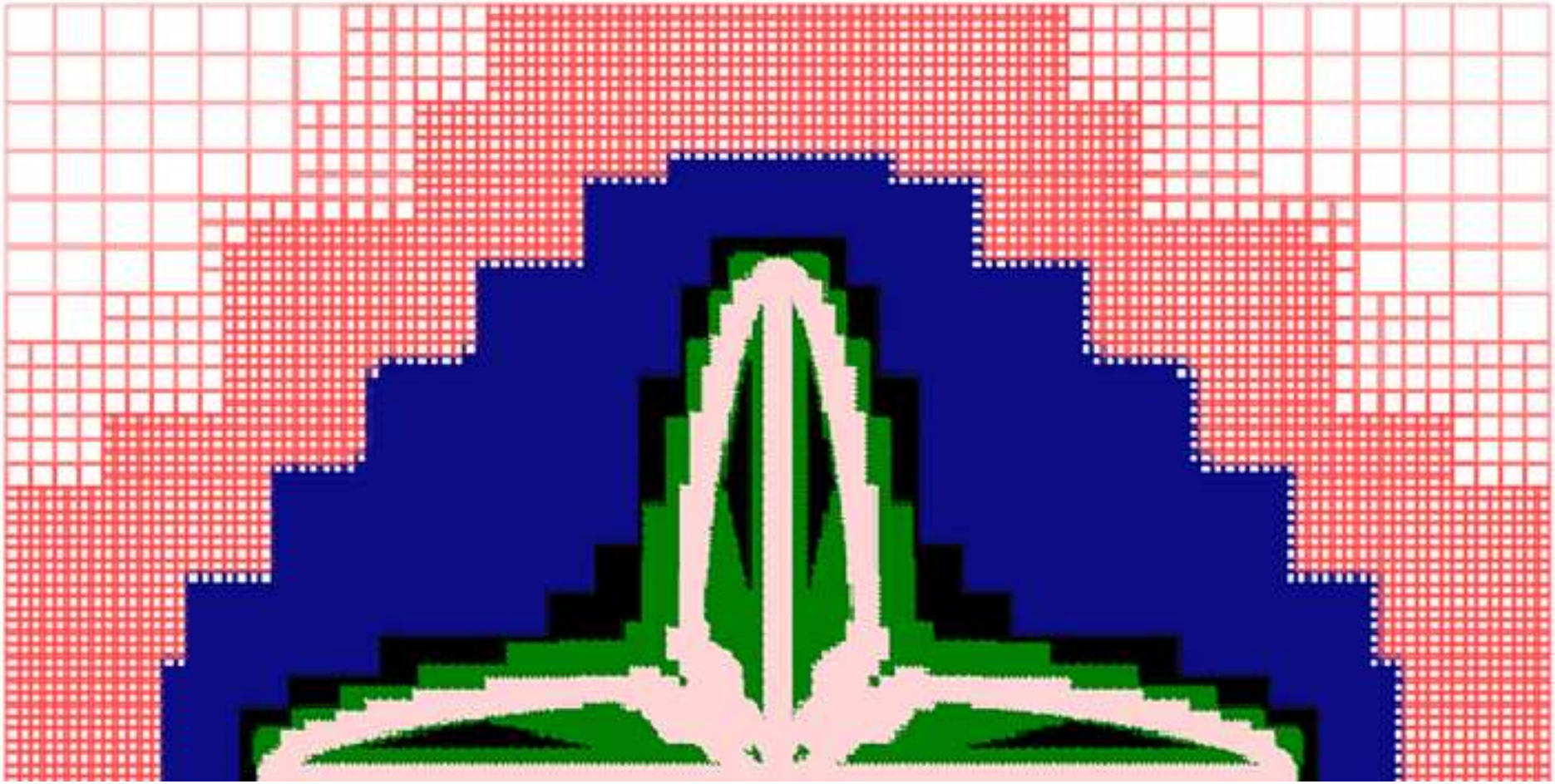

Figure 03, TIFF, LZW cmpress

Click here to download high resolution image

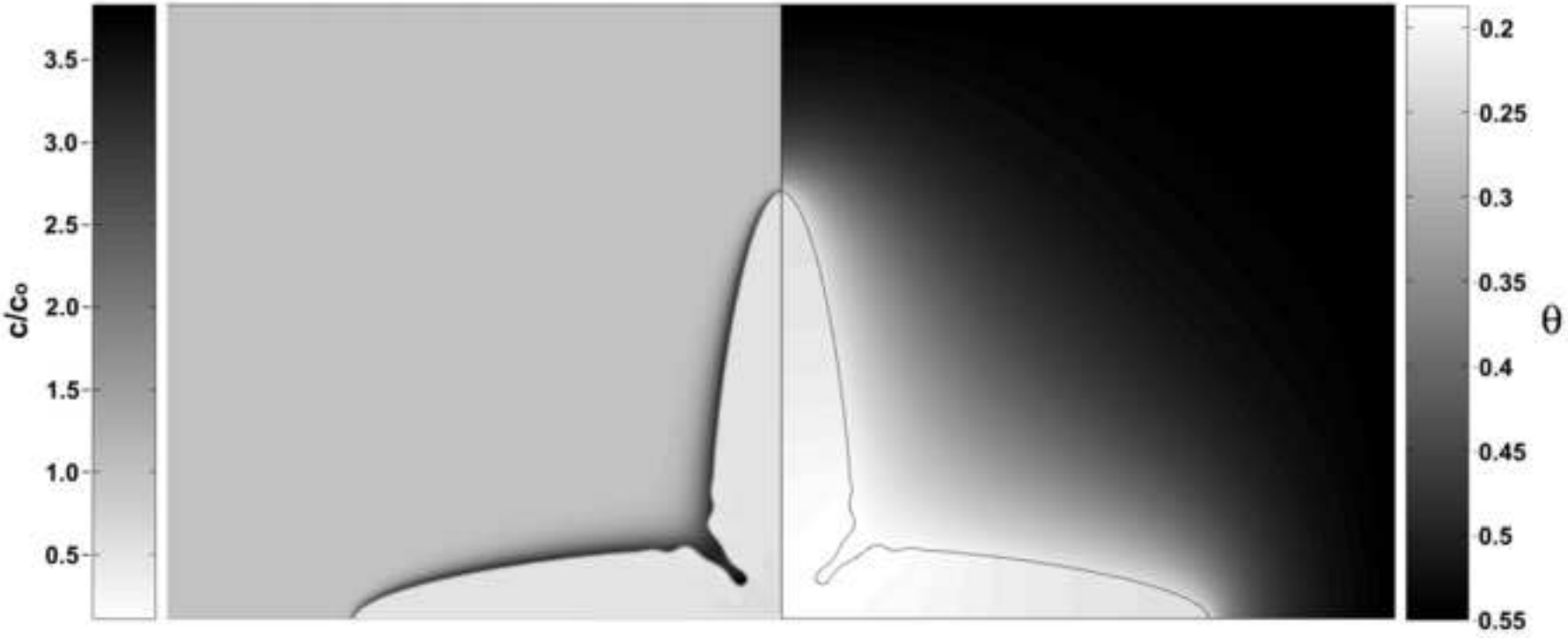

Figure 04, TIFF, LZW cmpress
Click here to download high resolution image

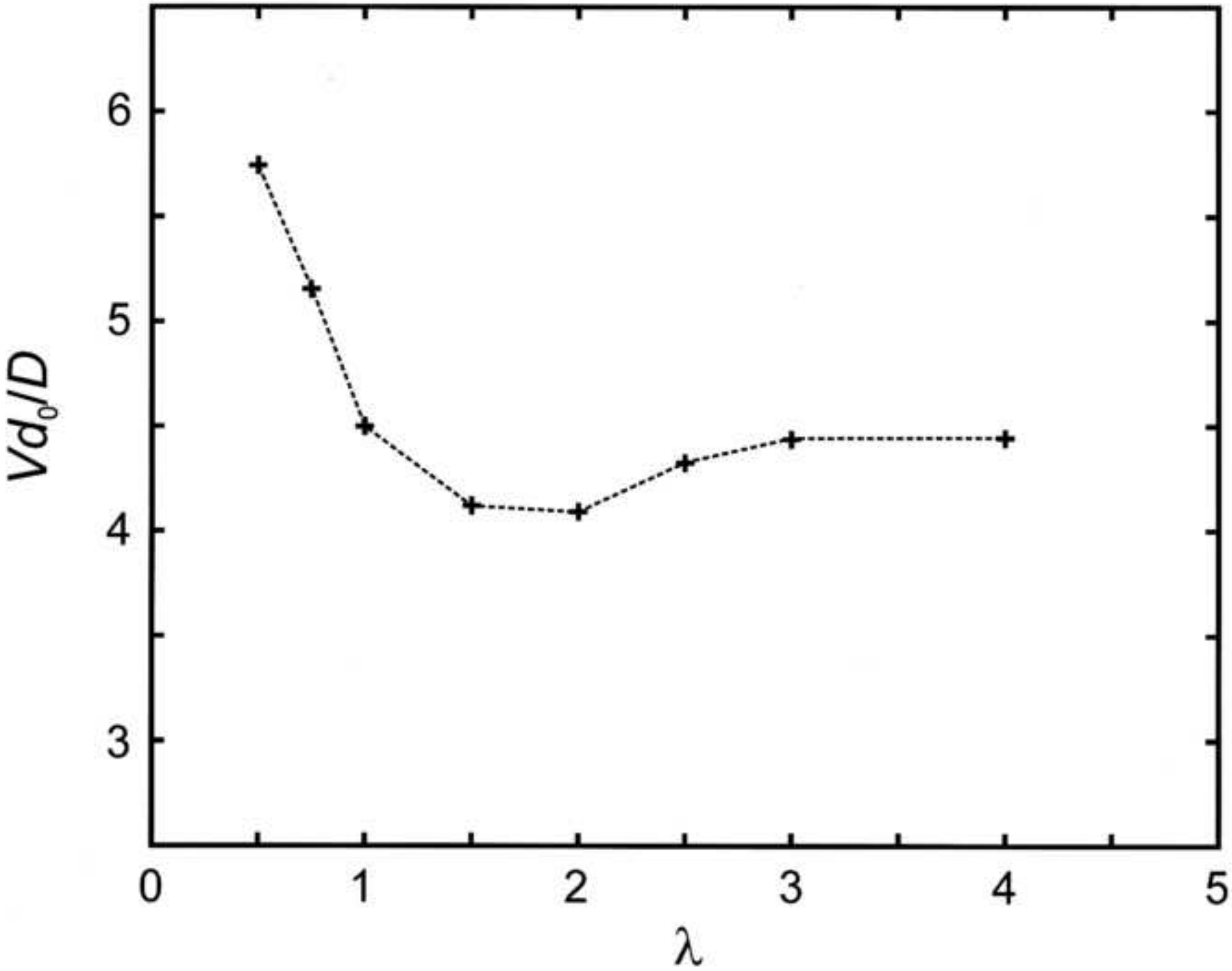

Figure 05, TIFF, LZW cmpress
Click here to download high resolution image

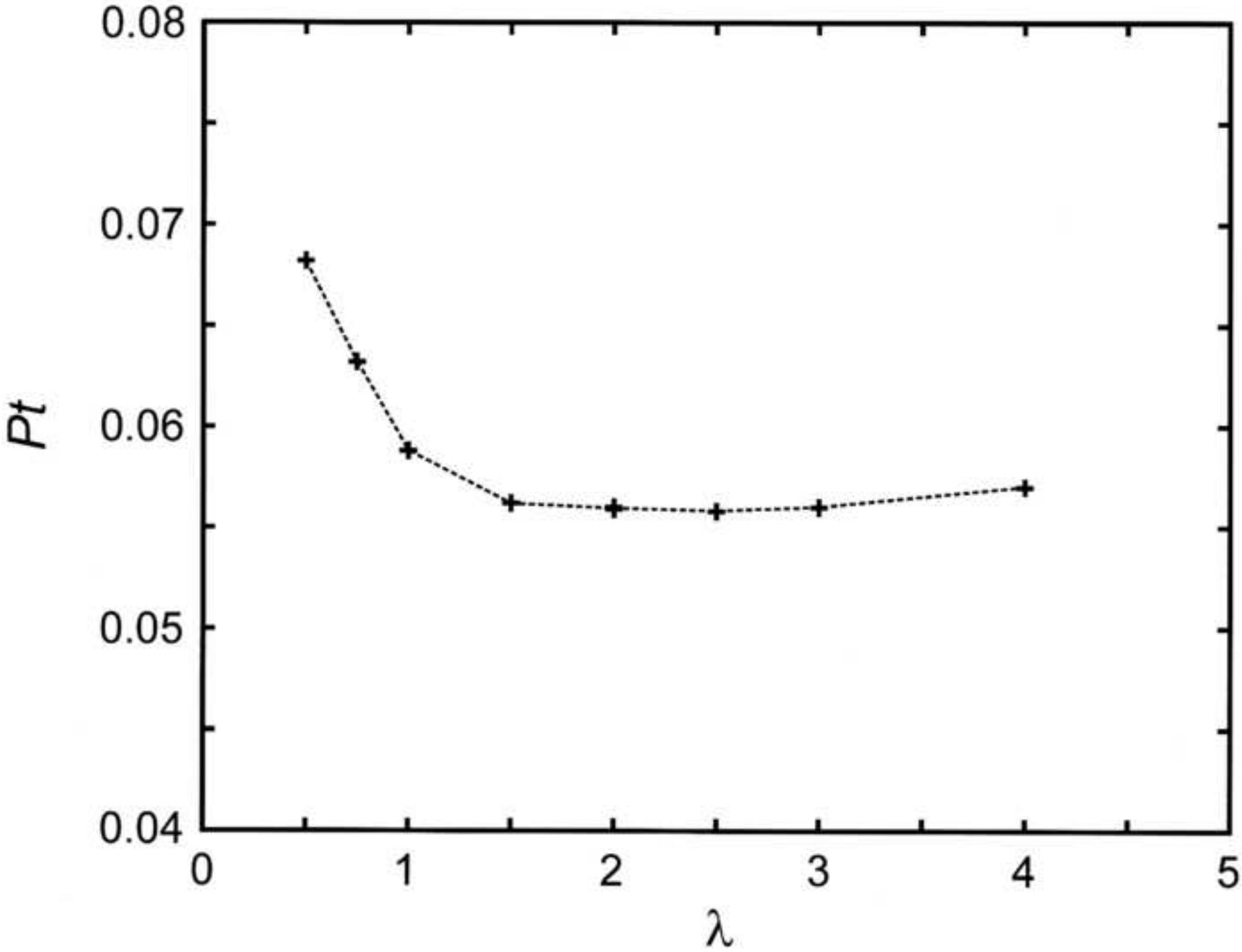

Figure 06, TIFF, LZW cmpress
Click here to download high resolution image

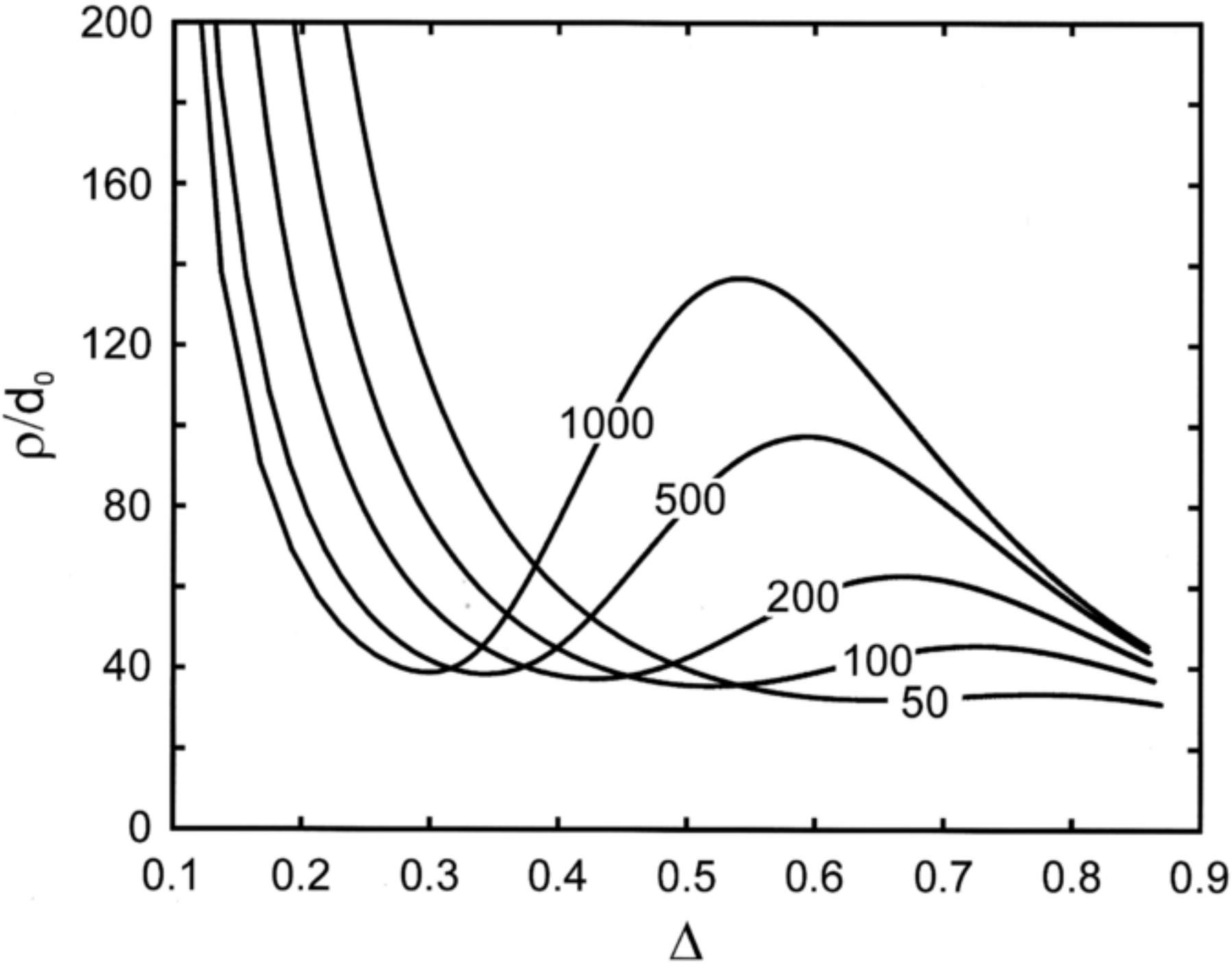

Figure 07, TIFF, LZW cmpress
Click here to download high resolution image

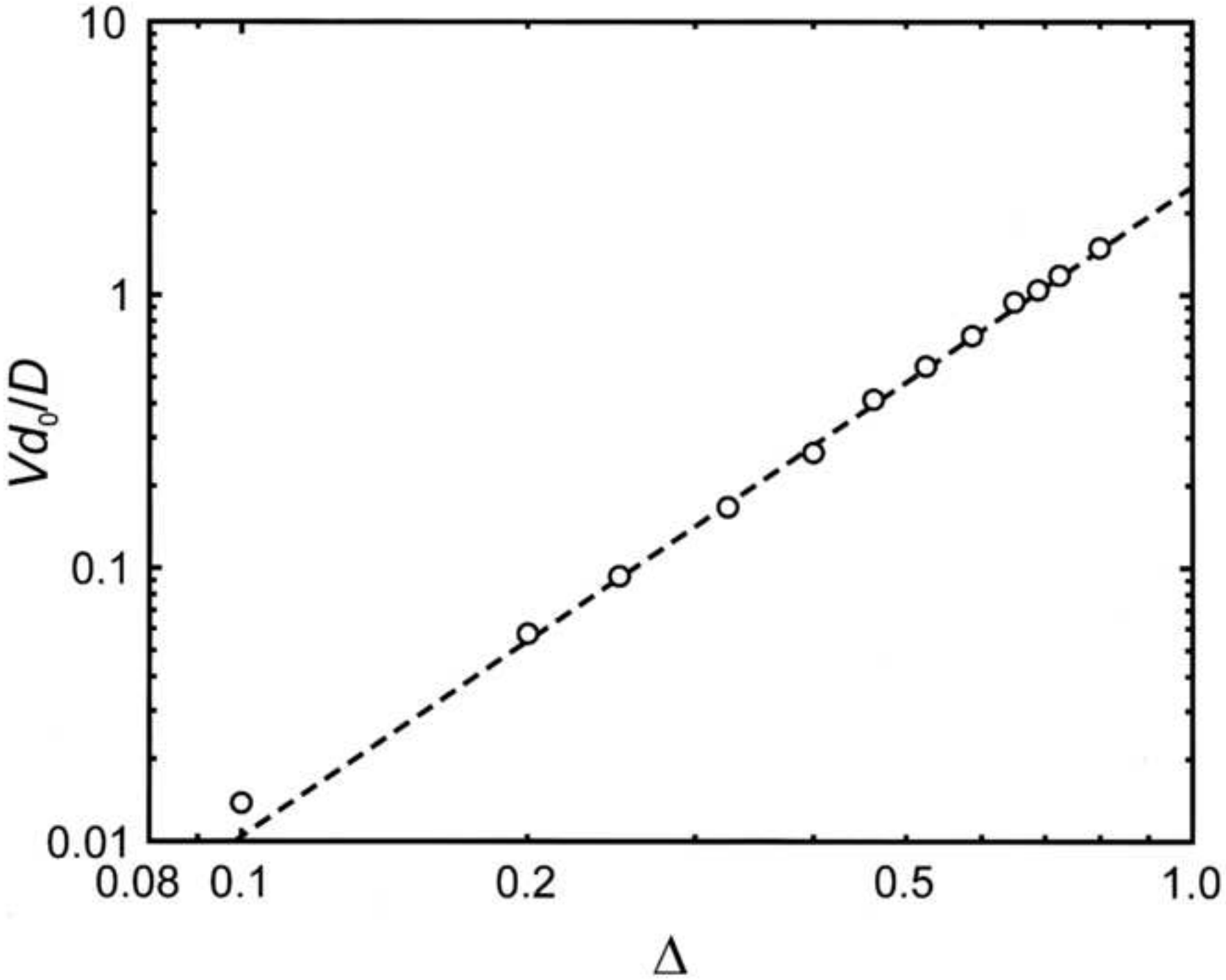

Figure 08, TIFF, LZW cmpress
Click here to download high resolution image

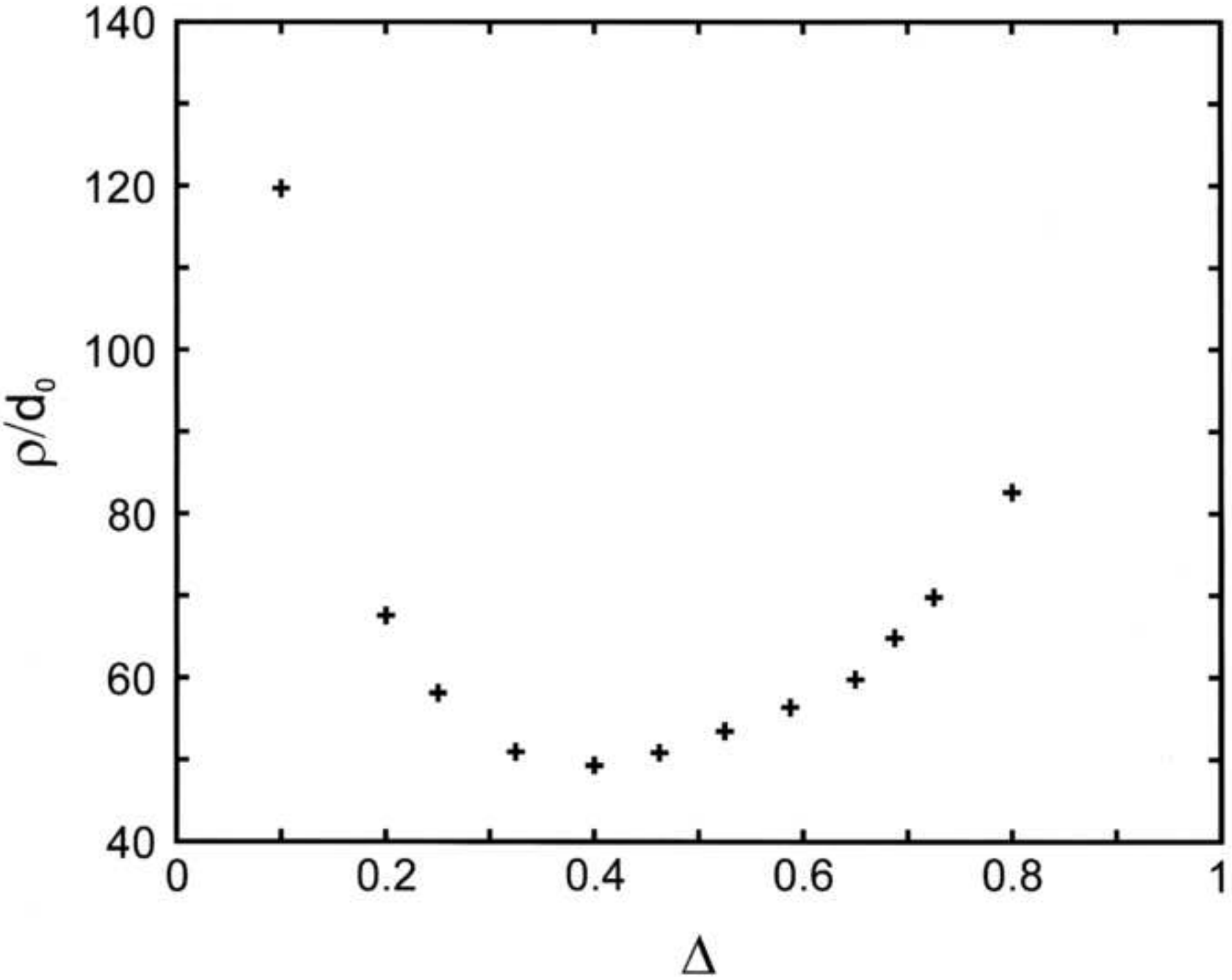

Figure 09, TIFF, LZW cmpress
Click here to download high resolution image

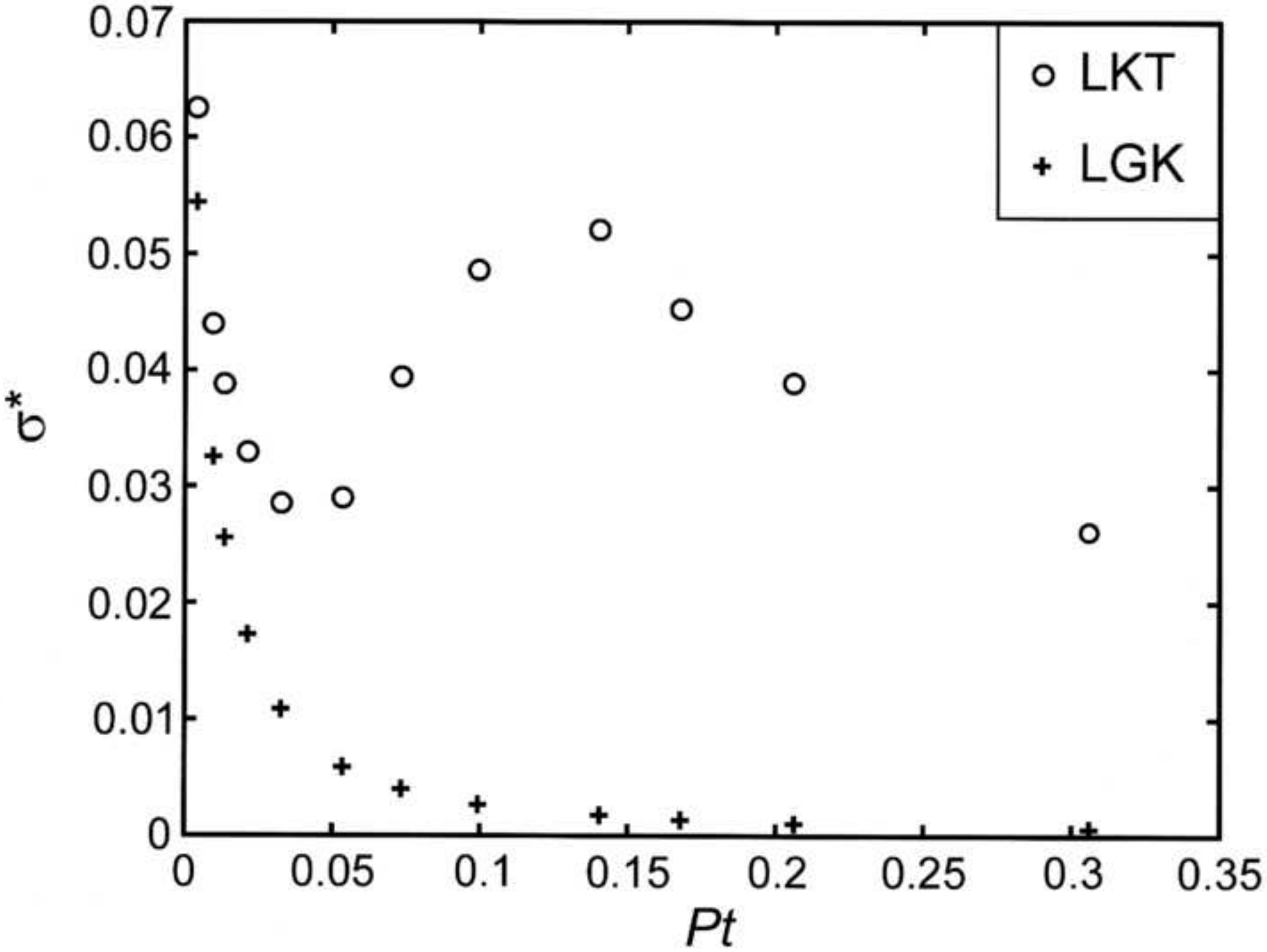

Figure 10, TIFF, LZW cmpress
Click here to download high resolution image